

Optimization of Dry Laser-Induced Graphene (LIG) Electrodes for Electrocardiography (ECG) Signals Monitoring

Denice Gerardo^{1,3}, Yann Houeix¹, Francisco J. Romero¹, Carmen L. Moraila^{1,4}, Isabel Blasco-Pascual², María Pérez-Cadenas^{5,6}, Diego P. Morales¹, Noel Rodriguez¹, Alfonso Salinas-Castillo^{2,*}

¹ Dept. Electronics and Computer Technology, Faculty of Sciences, University of Granada, Granada 18071, Spain.

² Dept. Analytical Chemistry, Faculty of Sciences, University of Granada, Granada 18071, Spain.

³ Facultad de Biología, University of Sinaloa, Culiacan, 80040, Mexico.

⁴ Facultad de Ciencias Físico-Matemáticas, University of Sinaloa, Culiacan, 80040, Mexico.

⁵ Department of Inorganic Chemistry and Technical Chemistry, UNED, Madrid 28232, Spain.

⁶ Dept. Inorganic Chemistry, Faculty of Sciences, University of Granada, Granada 18071, Spain.

* corresponding author, alfonsos@ugr.es

Available ORCID List: D.G. 0000-0002-7810-6345; Y.H. 0000-0002-1959-2187; F.J.R. 0000-0002-1582-9626; C.L.M. 0000-0002-6659-7781; I.B.P. 0000-0003-3997-9191; M.P.C. 0000-0001-8377-587X; D.P.M. 0000-0002-3294-8934, N.R. 0000-0002-6032-6921; A.S.C. 0000-0002-1360-6699.

Abstract

This work presents the optimization of the fabrication procedure for laser-induced graphene (LIG) electrodes intended for biopotentials acquisition. The results presented in this study demonstrate a significant improvement with respect to the performance obtained for other LIG-based electrodes previously reported in the literature. In particular, we propose the use of a galvanometric laser instead of a CNC laser to improve the engraving resolution and the LIG synthesis process, thus enhancing the surface area of the interface skin-electrode. For that, we have studied the resistance of the resulting LIG patterns as a function of the laser parameters (engraving power and scan speed) seeking their optimization. After tuning the laser fabrication process, we have fabricated and characterized electrocardiogram (ECG) electrodes with different surface areas using a commercial silver-based electrode as a reference. Thus, circular electrodes with a diameter of 15 mm, 10 mm and 6.5 mm were used to acquire the ECG on different volunteers using a commercial equipment. The signals acquired were processed afterwards with cutting edge processing techniques to perform a statistical analysis in terms of sensitivity, specificity, positive prediction and accuracy for the detection of QRS complexes. The results demonstrate that the proposed electrodes improve the signal acquisition with respect to the previously reported LIG-based electrodes in terms of noise and do present comparable or even better results than commercial electrodes (even with a smaller surface area) with the additional advantage of not requiring the use of an electrolyte gel.

Keywords: laser-induced graphene, electrocardiogram, flexible electronics, biosignals, electrodes, laser fabrication.

1. Introduction

Cardiovascular diseases (CVD) are the leading cause of death worldwide [1]. According to reports from the World Health Organization (WHO), there were 17.9 million of deaths associated with CVDs in 2019, representing the 32% of worldwide deaths. Furthermore, it is estimated that the number of CVD deaths will rise to 23.6 million per year by 2030 [2]. Consequently, significant efforts have been dedicated to the early diagnosis, prevention, and treatment of these diseases. Electrocardiography (ECG) plays a crucial role in this context, as it enables the early detection of CVDs by non-invasively monitoring the heart's electrical activity. Traditionally, acquiring an ECG required hospital visits and the use of complex monitoring systems. However, the advent of wearable health-monitoring systems (WHMS) have revolutionized this field [3]. These devices are expected to enable the ubiquitous monitoring of biological signals in a

imperceptible way, and for that, they must provide a high performance at the same time that they are affordable enough to reach the entire population [4].

Currently, the predominant materials used for manufacturing electrodes for electrocardiogram (ECG) acquisition, as well as for a wide range of other biosignals, are metals such as silver (Ag), copper (Cu), or gold (Au). Undoubtedly, these materials have demonstrated high performance in these applications [5]. Nevertheless, researchers from diverse interdisciplinary fields including biomedical engineering, chemistry, biology, physics, electronics, and materials science are collaborating to develop new materials that are not only compatible with human skin (providing attributes such as large area, softness, lightness, durability, flexibility, and biocompatibility) but also with inexpensive mass-production methods [6]. Therefore, different biocompatible materials with a large surface area have been proposed in recent years to enhance

the interface between the skin and the electrode. Among these materials we can stand out chemically-deposited (CVD) graphene, reduced graphene-oxide (rGO) or carbon nanotubes (CNTs), which have been produced on different plastic or textile substrates [7–10]. However, these proposed electrodes suffer from limited scalability due to the involvement of multiple and/or complex fabrication steps. More recently, laser-induced graphene (LIG) has been proposed for this application due to its inherent porous structure and straightforward synthesis (it can be induced directly on the surface of flexible substrates following a one-step laser process) [11,12]. The use of LIG for the fabrication of dry ECG electrodes was already reported, demonstrating that their performance could be comparable to that obtained with commercial Ag/AgCl electrodes [12]. The properties of the LIG make it an optimal candidate for the ECG acquisition since its fabrication process already involves obtaining a highly conductive material on a flexible polymer, which is a strategy commonly followed in the literature [13]. In addition, LIG is a highly thin and flexible material, which is essential for acquiring high-quality signals with low noise [14]. Moreover, despite its small thickness, LIG is a highly porous material with a large surface area [15], which also allows for increasing the contact surface with the human skin, thus reducing the skin contact impedance and improving the signal acquisition without the need of using electrolyte gels. These features not only simplify the fabrication procedure but also reduce production costs.

Recently, the research on the fabrication and characterization of LIG has experienced a considerable step forward, leading to multiple studies and publications focused on the optimization and application of this novel material [16,17]. In this context, this work presents the optimization of the synthesis process of LIG for the mass-production of high-quality ECG electrodes. For this purpose, we propose utilizing a high-performance industrial 532 nm diode laser driven by a galvanometer laser scanner. This kind of lasers, in contrast to CNC lasers, are optimized for engraving applications instead of cutting operations. Furthermore, their optical mechanism enables significantly higher resolution and engraving speed, thus improving the productivity in a large-scale manufacturing. Moreover, visible diode lasers are many times cheaper and offer higher spatial resolutions than infrared lasers and that is why they are expected to be wider used for the LIG fabrication in the near future [16,18]. The results presented in this work demonstrate that with this kind of laser allows sheet resistances lower than the obtained with low power UV laser diodes or CO₂ infrared lasers without compromising the porous morphology of the LIG, thus enhancing their performance as ECG electrodes.

The manuscript is structured as follows. After this introduction, Section 2 presents the materials and procedures employed for the fabrication and characterization of the different electrodes. Section 3 includes, on the one hand, the structural and electrical characterization of the LIG and, on the other hand, a comparison of the performance of the LIG electrodes for the ECG acquisition using different surface

areas. This section also contains a comparison with respect to commercial electrodes as well as with the previously reported LIG-based electrodes. Finally, Section 4 presents the main conclusions.

2. Materials and Methods

2.1. Electrodes fabrication

The initial precursor for the fabrication of LIG electrodes was polyimide films Kapton® HN (from 3D-Drucker-Filament.de, Berlin) with a total thickness of 60 μm (25 μm thick film and a 35 μm of adhesive). Prior to the laser ablation process the polyimide substrate was attached to a sheet of standard paper (0.09 mm thick) to provide greater consistency to the electrodes without compromising the electrode flexibility during the measurements. The paper also prevents the deformation of the polyimide as a consequence of the heat generated during the laser photothermal process. The surface was cleaned afterwards with isopropyl alcohol. The laser treatment was performed directly on the Kapton® HN surface (focal distance 270 mm) using the galvanometer laser Power Line E-12-532 from COHERENT with a wavelength of 532 nm (green) at ambient conditions. As no previous studies have explored the use of this type of laser for this purpose, we fabricated multiple samples using different laser powers and speeds (ranging from 0.5 W to 1 W and from 10 mm/s to 95 mm/s, respectively). The aim was order to identify the optimal configuration that would maximize the electrical conductivity of LIG while maintaining the integrity of the substrate.

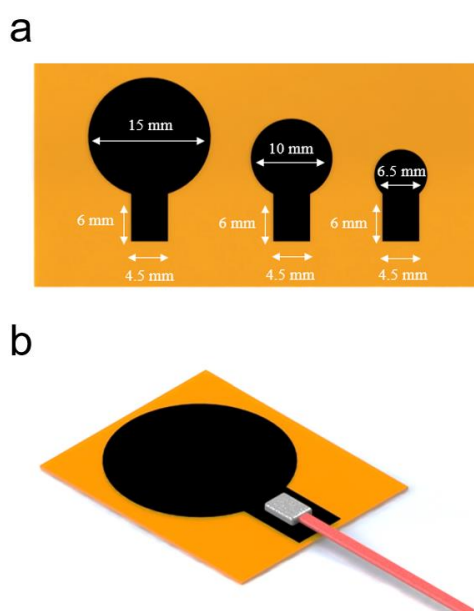


Fig. 1. (a) Schematic of laser-induced electrode patterns with different diameters (15 mm, 10 mm, and 6.5 mm) and their corresponding terminals. (b) Schematic representation of an electrode with the completed connection.

Once the parameters for the laser photothermal process were optimized, we fabricated round electrodes with three different diameters (15 mm, 10 mm and 6.5 mm), as shown in **Fig. 1a**. The round electrodes were endowed with a rectangular terminal to facilitate their connection with the ECG acquisition equipment. To achieve this, a cable was affixed to the terminal using a silver-based conductive ink (RS PRO Silver Conductive Paint from RS), as shown in **Fig. 1b**. Finally, the connection was lacquered to avoid its contact with the human skin during the ECG measurement process.

2.2. LIG characterization

The sheet resistance of the LIG obtained with the different laser configurations was measured following the four-point contact method at a constant current of 1 mA with a probe from Jandel connected to a B2901A Source Measurement Unit (SMU) from Keysight Technologies (Santa Rosa, California, USA). The NVision 40 field emission scanning electron microscope (SEM) from Carl Zeiss (Oberkochen, Germany) was used to acquire the SEM images at an extraction and acceleration voltage of 5kV. The Raman dispersive micro-spectrometer NRS-5100 from JASCO International Co. Ltd. (Tokyo, Japan) equipped with a green excitation source (Nd:YAG, $\lambda = 532$ nm) was used to obtain the Raman spectra. The Axis Ultra-DLD spectrometer from Katros Analytical Ltd. (Manchester, UK) was employed for the X-ray Photoelectron Spectroscopy (XPS); the measurements were performed at a base pressure of 10^{-10} Torr with an Al K α ($h\nu = 1486.6$ eV) excitation source at an operating power of 450 W. For the Diffuse Reflectance Infrared Spectroscopy (DRIFT) spectroscopy the resulting LIG was scratched from the surface of the polyimide to obtain a powder (~ 2 mg) that was mixed with anhydrous KBr (~ 200 mg) for its analysis in a Bruker Tensor 27 spectrometer (Bruker Co., MA, USA), as reported in previous works [19]. The specific surface area was obtained using nitrogen adsorption isotherms (77 K) with a ASAP2020 Brunauer-Emmett-Teller (BET) surface analyzer from Micromeritics Instrument (Georgia, USA). Before the measurements, ~ 75 mg of LIG powder were degassed in high vacuum at 150 °C for 10 h to remove any adsorbed species from the samples. Surface roughness characterization of the LIG samples were conducted using a white light confocal microscope from Sensofar Metrology (Terrassa, Spain) with a 20X objective covering an area of $694.41 \times 510.09 \mu\text{m}^2$.

2.3. Electrodes performance characterization

2.3.1. ECG Measurement setup

The performance of the proposed electrodes was studied in a comparative way with respect to commercial silver/silver-chloride (Ag/AgCl) electrodes (Ambu® BlueSensor VL model VL-00-S /25), as well as with respect to the previously

reported LIG-based electrodes, as described in [12]. ECG signals were acquired on the different volunteers using a Biosignals Researcher Kit portable body measurement device combined with three-lead local differential ECG electrodes (both from PLUX wireless biosignals S.A., Lisbon, Portugal). Two different acquisitions channels were simultaneously used to measure the ECG signals for the two types of electrodes being compared. The signals were sampled using a resolution of 16 bits at a sampling frequency of 1 kHz. The acquired signals were sent in real-time via Bluetooth to a personal computer for their subsequent analysis.

During ECG signal acquisition, the volunteer was seated forming a trunk-femur angle of 90° with the arms rested on a table. The electrodes were placed on the volunteer according to Einthoven's triangle lead I [20], i.e., two electrodes on each wrist (one of each type, with the positive electrodes on the left arm and the negative electrodes on the right) and a third electrode as a reference on the left ankle. The electrodes were attached to the subjects using adhesive fabric tape intended for medical purposes. For each pair of electrodes, the measurements were acquired consecutively on the different volunteers for at least 180 seconds. A total of 11 healthy subjects participated in the study, whose age and weight ranged between 22-40 years and 52-76 Kg, respectively.

2.3.2. Electrodes Performance Analysis

The acquired signals were processed using the algorithm proposed by Castillo *et al.* [21], intended for detecting the QRS complexes of the ECG signals with a great precision. This algorithm takes special interest because it is designed to be used in wearable health monitoring systems without requiring high computational features. Firstly, this algorithm applies the discrete wavelet transform (WDT, specifically Daubechies 9 - db9 - wavelet) to decompose the signal into nine different levels in the time–frequency domain, removes the low frequencies components (<1 Hz) and filters the contribution of the high frequencies (>16 Hz). This first step helps to remove the noise caused by skin-electrode contact and volunteer's movement as well as to filter the high frequency noise, especially the corresponding to the electrical network (50-60 Hz). Secondly, a clustering algorithm is applied to the WDT-filtered signal to classify the peaks which compose the signals into two groups: R peaks (from QRS complexes) and others (noise). This classification is done based on (1) the amplitude of the peak (maximum followed by a minimum) and (2) the time duration of the peak. Given that both ECG signals are acquired simultaneously and WDT-filtered under the same conditions (with the algorithm previously calibrated to maximize the results using commercial electrodes), the better the quality of the signal acquired, the better the classification.

On this basis, the performance of the different electrodes is evaluated as a function of the true positives and negatives

(TP , TN) and false positives and negatives (FP , FN) extracted from the visual inspection of the resulting ECG signal classification. The comparison is set in terms of sensitivity (Se), specificity (Sp), positive predictivity (PP) and accuracy (A) [22]:

$$Se(\%) = \frac{TP}{TP + FN} \cdot 100 \quad (1)$$

$$Sp(\%) = \frac{TN}{TN + FP} \cdot 100 \quad (2)$$

$$PP(\%) = \frac{TP}{TP + FP} \cdot 100 \quad (3)$$

$$A(\%) = \frac{TP + TN}{TP + TN + FN + FP} \cdot 100 \quad (4)$$

3. Results and Discussion

3.1. Synthesis of the LIG

As described in the methods' section, the LIG patterns were engraved on the surface of the polyimide (**Fig. 2a**) using the 532 nm galvanometer laser at different laser powers and scanning speeds (**Fig. 2b**). The alteration of the color of the polyimide when applying the laser photothermal process is clearly visible: the initial orange color of the Kapton[®] HN (**Fig. 1a**) turns into a dark gray color when LIG is produced on its surface. **Fig. 2c** and **Fig. 2d** shows that the laser is able to pattern the surface with a high resolution obtaining a homogeneous LIG layer on top of the surface with great adherence.

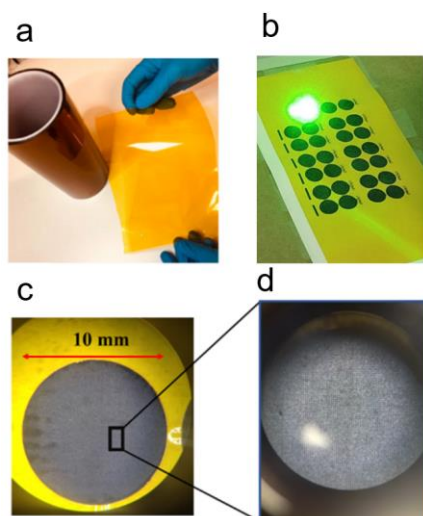


Fig. 2. a) Original polyimide films. b) Mass production of electrodes using the galvanometer laser. c) Zoom on one of the electrodes with a diameter of 10 mm. d) Zoom on the LIG area.

During the fabrication process it was demonstrated that if the laser fluence is too high (e.g., high laser power and low scanning speed), the surface of the polyimide starts to decompose. On the contrary, if ratio power/speed is too low, the laser fluence is not enough to surpass the ablation threshold [23].

3.2. Electrical characterization

For the electrical characterization of the LIG as a function of both laser power and speed, we fabricated multiple rectangular samples with 7 mm of width and 12 mm of length ranging the power from 0.5 W to 1 W and the scanning speed from 10 mm/s to 95 mm/s. The sheet resistance for the different laser powers is shown in **Fig. 3** as a function of the scanning speed. We have discarded those samples which did not reach the ablation threshold as well as those which were burned. An actual picture of the LIG samples obtained at the different laser powers and scanning speeds can be found in the supporting information (**Fig. S1**).

In general, the resistivity of the samples decreases as the ratio power/speed increases, which is associated with a higher laser fluence. As seen, as we increase the laser power (see power range 0.5 – 0.8 W), the ablation threshold can be achieved for higher scanning speeds, although resulting in greater values of sheet resistance. Moreover, the highest powers (0.9 W and 1 W) at intermediate scanning speeds result in a deteriorated LIG layer, thus also leading to higher sheet resistances.

On this basis, the optimum range of operation is between 0.5 W – 0.8 W and 10 mm/s – 70 mm/s, where sheet resistances as low as 20 Ω /sq. can be achieved, improving significantly the results reported for LIG synthesized from polyimides using UV visible lasers (which has been reported in the range 108 Ω /sq – 250 Ω /sq for different lasers and specific wavelengths [18,19]) as well as for CO₂ infrared lasers (which has been reported in the range from 18.5 Ω /sq to 100 Ω /sq, but for higher laser powers [15,24]). Based on these results, and also to streamline the fabrication process, we selected the configuration with a laser power of 0.7 W and a laser speed of 40 mm/s for the fabrication of the ECG electrodes.

3.3. Structural characterization

The SEM image of **Fig. 4a** shows the LIG-polyimide boundary after the laser photothermal process with the selected configuration, where we can clearly identify the edge between the laser-irradiated area (on the left), presenting the porous morphology as a result of the LIG production, and the flat homogeneous non-irradiated polyimide (on the right).

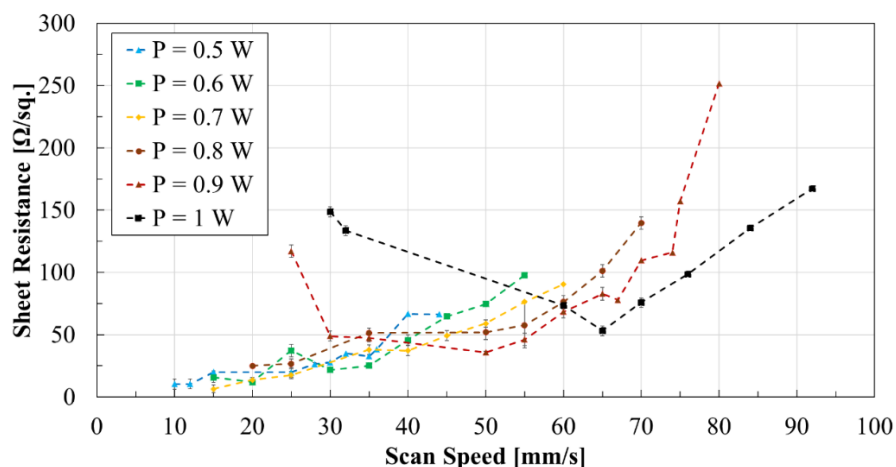


Fig. 3. Sheet resistance of different LIG samples fabricated at different laser powers and scanning speeds. Inset shows the measurement setup for the different samples.

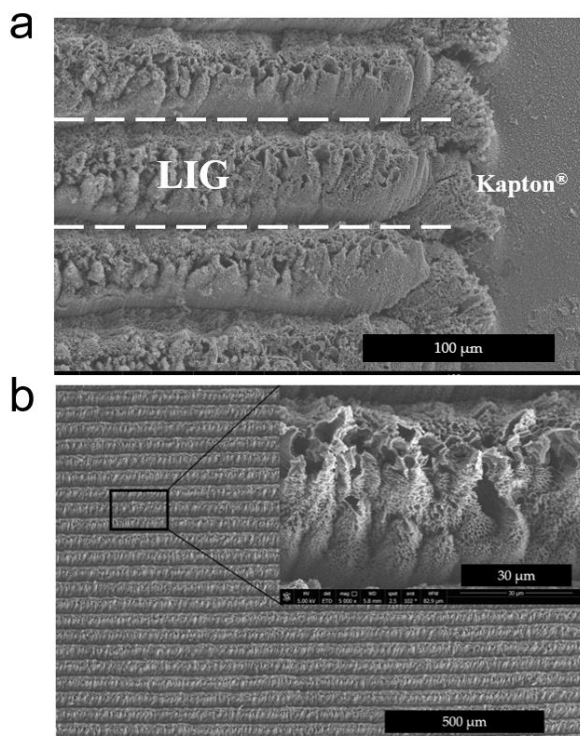


Fig. 4. SEM images: (a) Edge between the laser-irradiated and non-irradiated area – Scale bar: 100 μm , (b) LIG electrode surface – Scale bar: 500 μm (inset shows a magnification of the surface – Scale bar: 30 μm).

Moreover, we can see in the SEM image of **Fig. 4b** that the electrode is patterned on the surface in the form of horizontal superposed lines with a step between consecutive laser passes of $\sim 50 \mu\text{m}$. These images demonstrate that this new fabrication setup avoids the formation of the mesh-like structures derived from the mechanical step resolution of some CNC lasers, as reported in [12]. Lower laser fluences,

as shown in supplementary **Fig. S2a** for a laser power of 0.6 W and scanning speed of 50 mm/s, result in a thinner LIG formation over the surface of the polyimide with untreated regions in between the scribed LIG lines. Moreover, increasing the ratio power/speed far beyond the ablation threshold (as shown in **Fig. S2b** for a laser power of 0.7 W and a scanning speed of 15 mm/s) leads to the appearance of imperfections in the LIG layer as a consequence of a severe thermal deformation of the LIG structure, as also shown in **Fig. S1**. Therefore, the selected configuration allows for achieving a homogeneous porous layer of LIG with high available surface area and a low sheet resistance while preserving the integrity of the substrate. In particular, BET experiments indicate that the resulting material presents a specific surface area of $220 \pm 1 \text{ m}^2/\text{g}$, which is similar or even larger than other LIG obtained from polyimides [25,26]. In addition, the foam-like structure of the LIG is of special interest for our target application over other alternative two-dimensional (2D) forms of graphene due to this available surface area [27,28]. For instance, the surface roughness experiments demonstrated that the LIG layer on the polyimide offers an available surface area of 0.6772 mm^2 for a projected area of 0.3553 mm^2 (in contrast to the 0.3773 mm^2 obtained on the polyimide surface for the same projected area). This high available surface area allows for a conformal contact when the electrode is pressed onto the skin, thus contributing to improve the acquisition performance by minimizing motion artifacts and reducing background noise [29,30].

Raman and XPS spectroscopies confirmed that the synthesized material is really a graphene-derived material. On the one hand, the wide XPS analysis of **Fig. 5a** and **Fig. 5b** demonstrates that the material obtained on the surface of the polyimide is composed mainly of carbon as a result of the breakdown of the carbon-oxygen compounds (and carbon-nitrogen to a lesser extent) that compose the original structure of the Kapton[®] polyimide films, thus leading to a

notable increase of the C/O atomic percentage ratio (as seen in **Table 1**). The level of carbon isolation achieved with this fabrication setup, which results in a 96.54% of carbon, is also higher than the achieved by other lasers used in the literature [25,31–35].

Table 1. Atomic concentrations of carbon, oxygen and their ratio obtained from the XPS results.

Material	Carbon content (%)	Oxygen content (%)	Relation C/O
Kapton® HN	76.36	16.72	4.57
LIG	96.54	2.02	47.79

From the results of the high-resolution carbon peak of the XPS spectra (**Fig. 5c** and **Fig. 5d**) and the DRIFT spectroscopy before and after the laser photothermal process (**Fig. 6a**), we can attribute the increment in the carbon percentage mainly to the removal of the imide (O=C-N-C=O) bonds which compose the polyimide structure [36]. This is manifested in the decrease of the C-N and C=O contributions in the XPS C1s peak, as well as in the decrease

of the intensity associated with the C-N (1112 cm^{-1}) and C=O (1712 cm^{-1}) bands of the DRIFT spectra after the laser photothermal process [37,38]. On the other hand, the Raman spectrum (**Fig. 6b**) reveals the graphene-derived nature of this material, as manifested by its main three peaks. In particular, the G peak, located at $\sim 1580\text{ cm}^{-1}$, is associated with the sp^2 hybridized carbon networks of graphitic materials, the D peak ($\sim 1345\text{ cm}^{-1}$) reveals the presence of defects in this structure (so it would be inexistent in pure single-layer graphene), and the 2D peak located at $\sim 2700\text{ cm}^{-1}$ is of particular interest for the study of the multilayer nature of these materials. For instance, in pure single-layer graphene, the intensity of the 2D peak is usually two or three times the intensity of the D peak and this ratio decreases as the number of layers of graphene increases [39]. Therefore, the results obtained for these LIG electrodes indicate that, although the samples present a high electrical conductivity, they also feature a higher defective and disordered structure (i.e., lower crystallographic quality). This can be attributed to the presence of sp^3 -hybridized carbon structures along with the sp^2 -hybridized carbon bonds responsible for the electrical conductivity, as well as to other imperfections and defects in the arrangement of carbon atoms, such as micropores, nanopores, and the presence of remaining oxygen-containing functional groups within the structure [16,40].

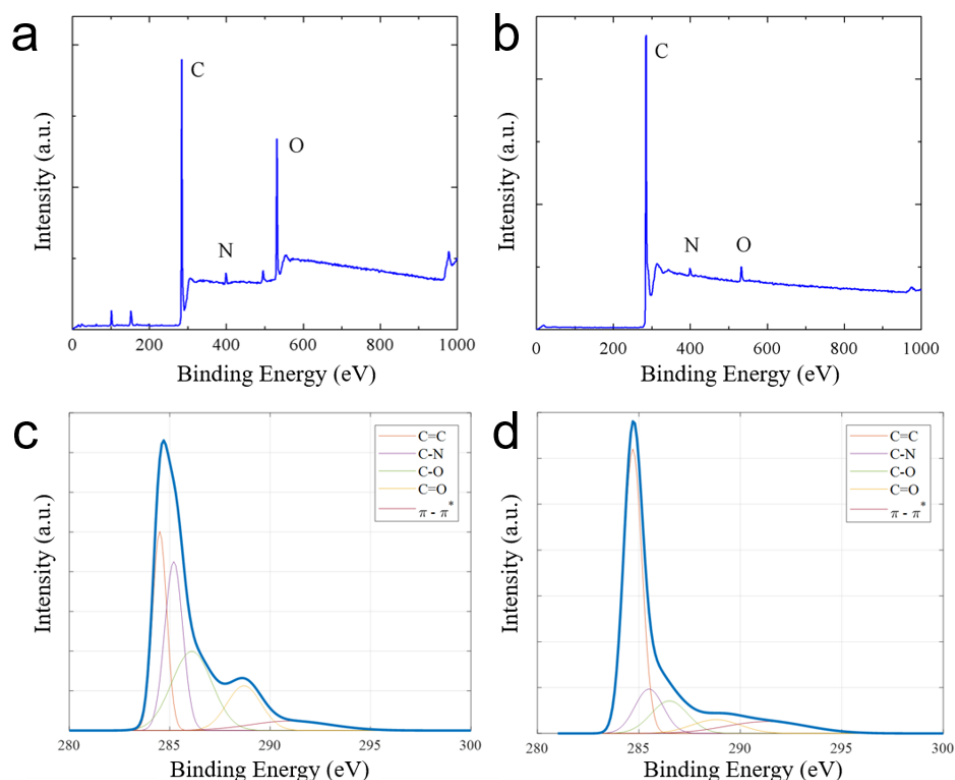


Fig. 5. Wide XPS spectra of the original Kapton® HN polyimide (a) and LIG (b). The peaks correspond to the contribution of the carbon (C), nitrogen (N) and oxygen (O). High-resolution XPS spectra of the carbon peak together with the decomposition into their main components before (c) and after (d) the laser photothermal process.

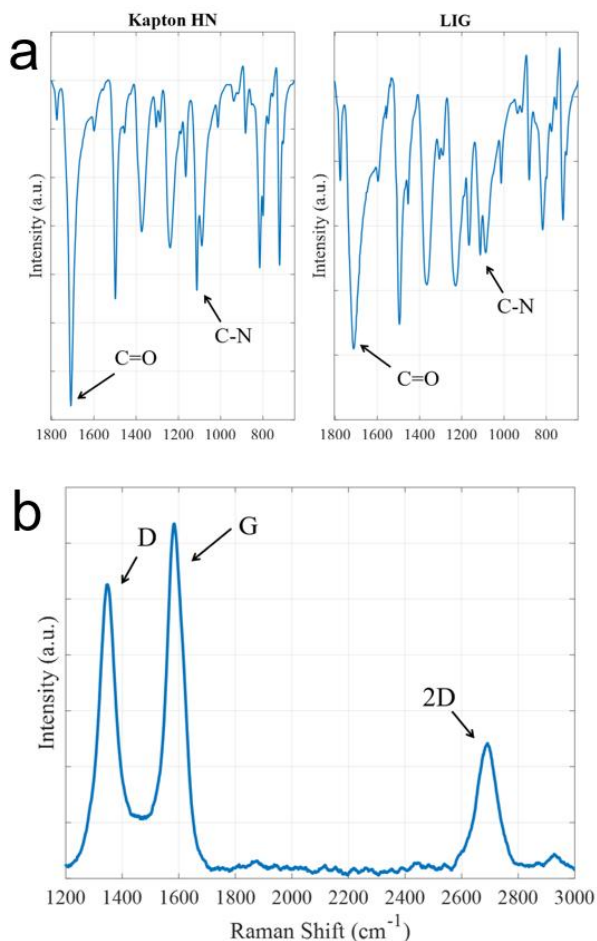


Fig. 6. a) DRIFT results for the Kapton[®] HN films and LIG powder with the identification of the most affected bands by the laser photothermal process. a) Raman spectrum of the LIG with its distinctive peaks at $\sim 1345\text{ cm}^{-1}$ (D peak), $\sim 1580\text{ cm}^{-1}$ (G peak), and $\sim 2700\text{ cm}^{-1}$ (2D peak).

3.4. ECG electrode performance

As detailed in Section 2.3, the ECG signals were acquired on the different volunteers with both the LIG-based and commercial Ag-based electrodes simultaneously to establish a reliable comparison between electrodes, given that the quality of the signal acquired can differ from one person to another as a function of their skin moisture level or body mass index [41]. An example of the raw signals extracted from the two channels of the Biosignals PLUX acquisition equipment can be seen in **Fig. 7**, for both LIG and commercial Ag/AgCl electrodes.

In both cases the ECG signals are composed by the characteristic P-QRS-T waves, together with low frequency noise (offset and wandering) and, mainly, 50 Hz noise as a consequence of the electronic network and surrounding electronic equipment, as shown in the raw signal of **Fig. 8**. This figure also shows the same signal after the WDT filtering, which is the one used afterwards by the clustering algorithm for the QRS complexes detection. As seen, the WDT filtering removes the offset of the signal (resulting in a signal centered in 0 V) and reduces the baseline wandering without disturbing the information contained in the key bands.

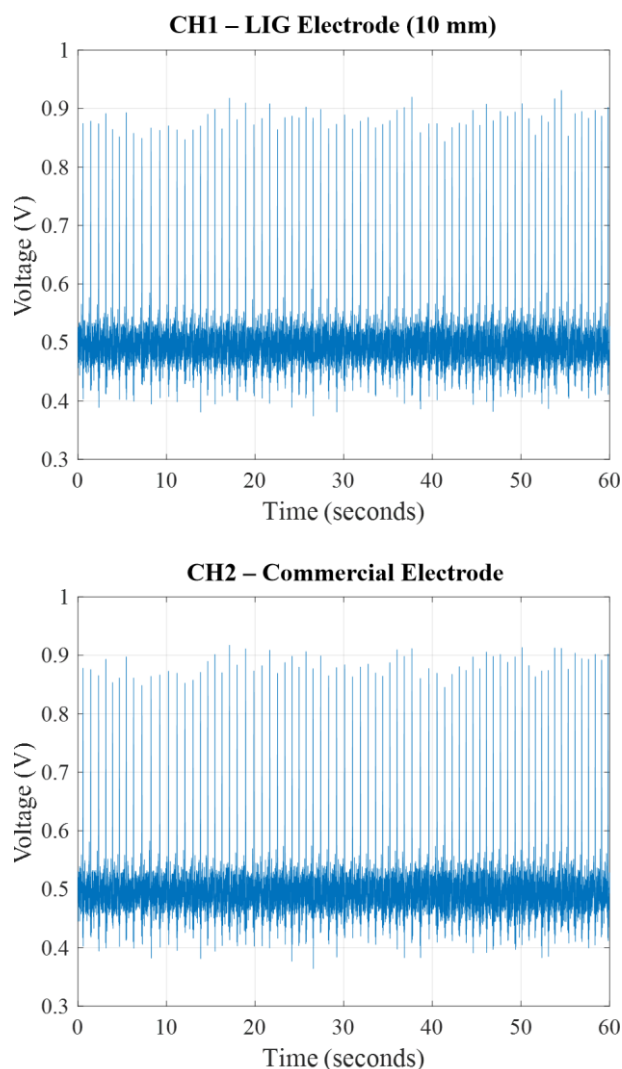


Fig. 7. Raw ECG signals recorded with the acquisition equipment using two channels, one for each type of electrode.

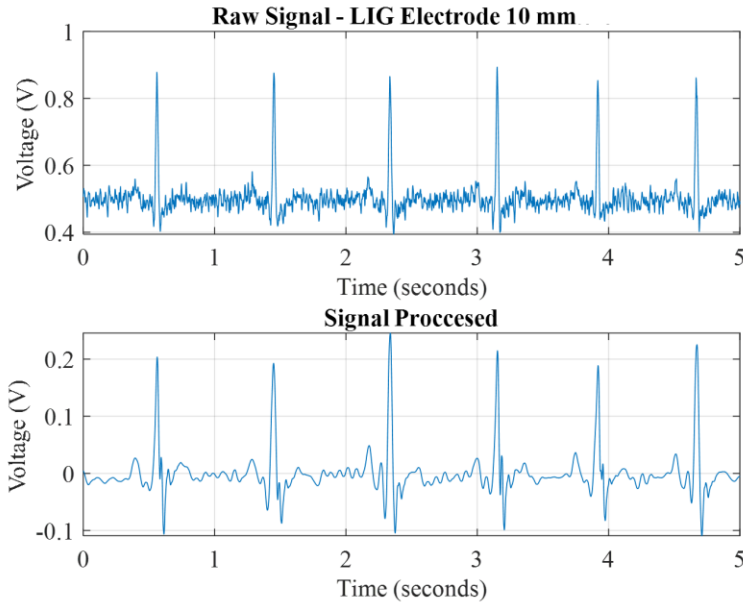


Fig. 8. Raw signal acquired using the LIG electrode with a diameter of 10 mm (top) and signal after the wavelet processing (bottom).

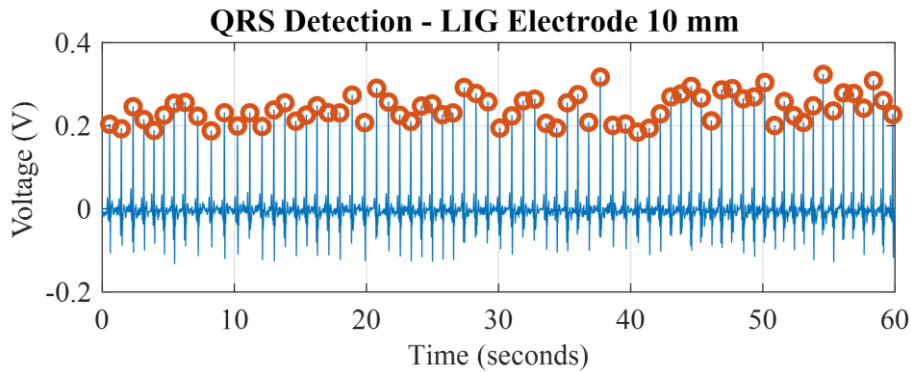


Fig. 9. Example of QRS complexes detection. The blue signal corresponds to the electrocardiogram over time and the red circles to the R peaks (from the QRS waves) detected by the algorithm after the signal processing (filtering and clustering).

After the filtering, the clustering algorithm classifies the peaks that compose the signals into two groups: QRS complexes and noise. An example of the output of this algorithm is depicted in **Fig. 9**, where each circle represents the R-peak of QRS complexes detected. Note that this method enables a more robust detection than if we consider the use of a fixed amplitude threshold value, since it would not be easy to ensure any selected value of threshold is the most appropriate for the different signals or volunteers [21]. This kind of classification is useful, for instance, to extract the heart rate of the subject.

In order to get the comparison for the different electrodes we processed the signals acquired simultaneously and extracted their true/false positives and true/false negatives. After that, we calculated the different performance parameters described in Section 2.3.2. This was done for the LIG-based electrodes with the three different surface areas (6.5 mm, 10 mm and 15 mm) to evaluate their performance with respect to the commercial electrodes. The results obtained are reported in the following tables (**Table 2 – Table 4**), where each value corresponds to the average value and standard deviation for the different volunteers. A graphical representation of these results is also shown in **Fig. 10**.

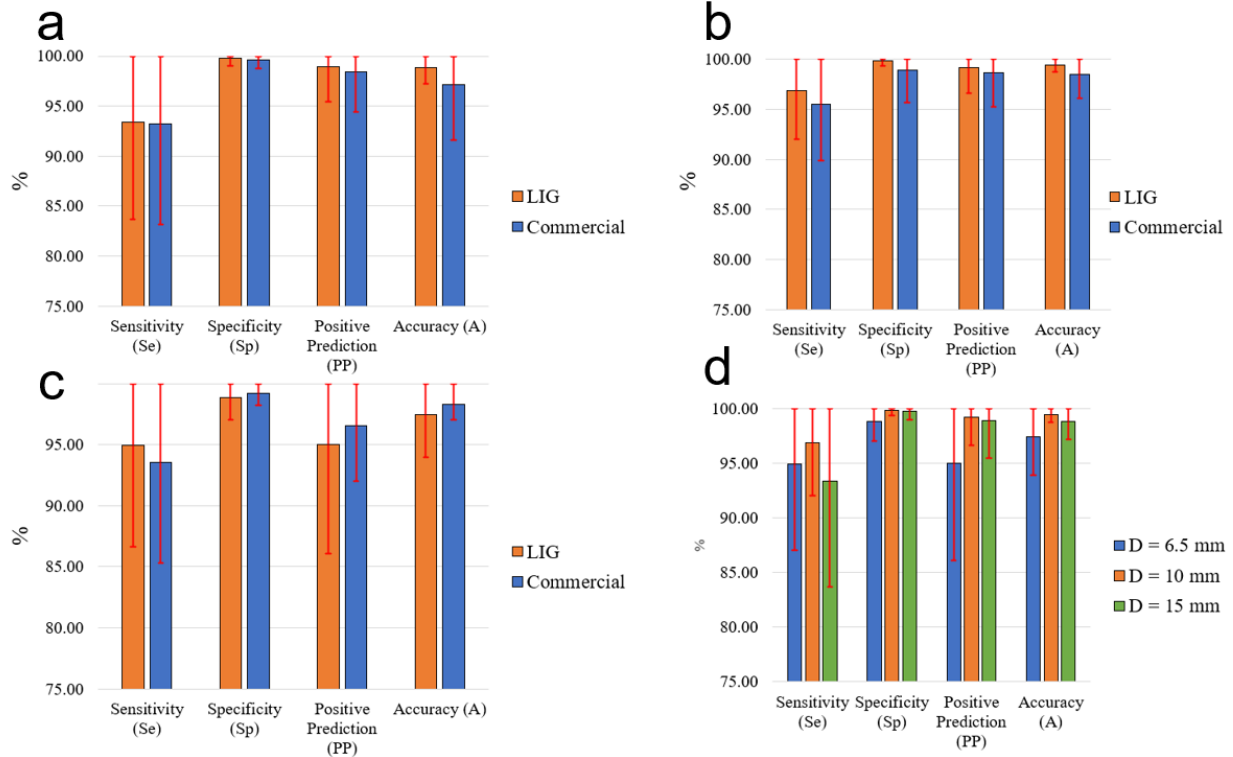


Fig. 10. Graphical representation of the results obtained for the performance parameters compared with the commercial electrodes for the LIG-based electrodes with the different diameters, (a) 15 mm, (b) 10 mm, (c) 6.5 mm, (d) comparison between the three LIG electrodes.

Table 2. Performance parameters for the 15 mm LIG electrodes compared with the commercial electrodes.

	LIG 15 mm	Commercial
Sensitivity (Se)	93.4 ± 9.1	93.3 ± 9.6
Specificity (Sp)	99.8 ± 0.7	99.7 ± 0.9
Positive Prediction (PP)	98.9 ± 3.3	98.5 ± 3.8
Accuracy (A)	98.8 ± 1.5	97.2 ± 5.3

Table 3. Performance parameters for the 10 mm LIG electrodes compared with the commercial electrodes.

	LIG 10 mm	Commercial
Sensitivity (Se)	96.9 ± 4.6	95.5 ± 5.3
Specificity (Sp)	99.9 ± 0.5	98.9 ± 3.1
Positive Prediction (PP)	99.2 ± 2.4	98.7 ± 3.2
Accuracy (A)	99.5 ± 0.7	98.5 ± 2.3

Table 4. Performance parameters for the 6.5 mm LIG electrodes compared with the commercial electrodes.

	LIG 6.5 mm	Commercial
Sensitivity (Se)	95.0 ± 7.9	93.5 ± 7.8
Specificity (Sp)	98.8 ± 1.7	99.2 ± 0.9
Positive Prediction (PP)	95.0 ± 8.5	96.5 ± 4.3
Accuracy (A)	97.5 ± 3.3	98.3 ± 1.2

As seen, the electrodes with greater area (10 mm and 15 mm) have a superior overall performance when compared with the commercial electrodes. Also note that the 6.5 mm electrodes, even with a smaller area, have a higher sensitivity than both commercial electrodes and 15 mm ones, although the rest of the performance parameters are slightly lower. This means they are able to capture effectively the multiple peaks that compose the signal but also that the quality of the acquired signal makes more difficult the classification of these peaks, thus leading to lower accuracy, specificity and positive prediction. Increasing the electrode size from 6.5 mm to 10 mm results in a higher electrode performance, which can be attributed to the larger contact area between the

electrode and the skin. Furthermore, the 10 mm diameter electrodes are the ones which offer the best results over both commercial and the other LIG-based electrodes. The fact of obtaining better results with these electrodes, even over those with a higher diameter (15 mm), is associated to the fact they feature less noise than larger electrodes at the same time that they are attached easily to a relatively flat part of the body [41].

In addition, we have also demonstrated that the optimized fabrication procedure proposed in this work allows for obtaining LIG-based electrodes with a better performance to that obtained with the previously reported LIG-based electrodes synthesized with a low-power CNC UV laser [12]. For that, we have fabricated additional LIG electrodes with a diameter of 10 mm using the laser and procedure described in [13]. The results shown in **Fig. 11** proves that the signal acquired with the optimized LIG electrodes proposed in this work present much less noise when compared with the LIG electrodes synthesized with the CNC UV laser.

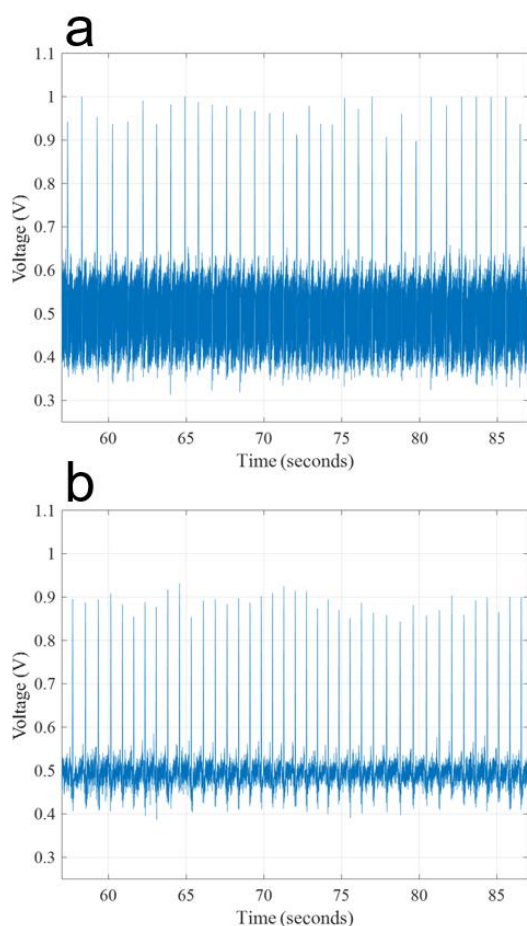


Fig. 11. ECG signal noise for both electrodes a) LIG electrodes synthesized with the UV laser, b) LIG electrodes synthesized with the green galvanometer laser.

In short, based on the results presented in this work, if we consider the different advantages of the proposed electrode, such as their performance (higher or at least similar than the obtained with commercial electrodes), their simple and inexpensive manufacturing process, their flexibility and the non-use of electrolyte gel; this fabrication procedure constitutes a potential alternative for the replacement of current commercial electrodes in the electronic biomedical monitoring devices of the near future.

4. Conclusions

This work presents an inexpensive method for the mass-production of high performance dry LIG electrodes over flexible polyimides intended for ECG acquisition. In particular we proposed the use of an industrial galvanometric laser with a wavelength of 532 nm which has been tuned to obtain a high quality LIG with better electrical conductivity than the reported for other lasers employed in the literature. This higher electrical conductivity is achieved without compromising the porous morphology of the LIG, which helps to enhance their performance as ECG electrodes. The performance of the proposed electrodes has been evaluated and compared with respect to commercial Ag/AgCl electrodes for different electrode's sizes. Using cutting-edge processing algorithms intended for the detection of the QRS complexes that compose the ECG signal we have demonstrated that these electrodes exceed the performance of the commercial electrodes in terms of sensitivity, specificity, positive prediction and accuracy with the additional advantage of not requiring the use of electrolyte gel to improve skin-electrode contact. It is also demonstrated that these electrodes improve the signal acquisition with respect to the previously reported LIG-based electrodes. Therefore, the fabrication procedure presented in this work paves the way for a viable and low-cost mass production of electrodes to be used not only in ECG monitoring devices, but also in other of health monitoring systems applications, such as electromyography or electrooculography.

Acknowledgements

This work was supported by the Grant PID2020-117344RB-I00 funded by MCIN/AEI/10.13039/501100011033, also by FEDER/Junta de Andalucía-Consejería de Transformación Económica, Industria, Conocimiento y Universidades Projects P20_00265 and BRNM-680-UGR20; Project TED2021-129949A-I00 funded by MCIN/AEI/10.13039/501100011033 and by European Union NextGenerationEU/PRTR; In addition, this work was also supported by the Junta de Andalucía – Consejería de Transformación Económica, Industria, Conocimiento y Universidades through the project ProyExcel-00268 as well as by the Spanish Ministry of Sciences and Innovation through the the María Zambrano fellow C21.I4.P1 and the predoctoral grant PRE2021-096886. This work has also been partially funded by the National Council of Science and

Technology CONACYT (grant number: 777736) and the Iberoamerican University Association of Postgraduate (AUIP) by means of the program “Mobility Program among all the institutions associated to the AUIP”.

Author contributions

Denice Gerardo: Investigation, Methodology, Validation, Writing – original draft.

Yann Houeix: Investigation, Methodology, Validation, Writing – original draft.

Francisco J. Romero: Investigation, Conceptualization, Formal analysis, Validation, Writing – original draft, Funding acquisition.

Carmen L. Moraila: Investigation, Methodology, Validation, Writing – review and editing.

Isabel Blasco-Pascual: Investigation, Methodology, Validation, Writing – original draft.

María Pérez-Cadenas: Investigation, Methodology, Resources, Writing – review and editing.

Diego P. Morales: Resources, Supervision, Funding acquisition.

Noel Rodriguez: Supervision, Resources, Writing – review & editing, Project administration

Alfonso Salinas-Castillo: Supervision, Resources, Writing – review & editing, Project administration.

Declarations

Funding and/or Conflicts of interests/Competing interests. The authors declare that they have no known competing financial interests or personal relationships that could have appeared to influence the work reported in this paper.

Data availability

Data will be made available from the corresponding author upon reasonable request.

References

1. S. Gehr, N. K. Balasubramaniam, and C. Russmann, *Nat Med* **29**, 781 (2023).
2. A. G. Sánchez-Arias, M. E. Bobadilla-Serrano, B. Dimas-Altamirano, M. Gómez-Ortega, and G. González-González, *5* (2016).
3. S. Zhang, S. Li, Z. Xia, and K. Cai, *J. Mater. Chem. B* **8**, 852 (2020).
4. H. Yang, J. Yu, H. Zo, and M. Choi, *Telematics and Informatics* **33**, 256 (2016).
5. V. L. da S. N. Button, *Principles of Measurement and Transduction of Biomedical Variables* (Elsevier/AP, Academic Press is an imprint of Elsevier, Amsterdam ; New York, 2015).
6. K. Erickson, R. Erni, Z. Lee, N. Alem, W. Gannett, and A. Zettl, *Advanced Materials* **22**, 4467 (2010).
7. N. Celik, N. Manivannan, A. Strudwick, and W. Balachandran, *Nanomaterials* **6**, 156 (2016).
8. C. Lou, R. Li, Z. Li, T. Liang, Z. Wei, M. Run, X. Yan, and X. Liu, *Sensors* **16**, 1833 (2016).
9. N. Karim, S. Afroj, A. Malandraki, S. Butterworth, C. Beach, M. Rigout, K. S. Novoselov, A. J. Casson, and S. G. Yeates, *J. Mater. Chem. C* **5**, 11640 (2017).
10. H.-C. Jung, J.-H. Moon, D.-H. Baek, J.-H. Lee, Y.-Y. Choi, J.-S. Hong, and S.-H. Lee, *IEEE Trans Biomed Eng* **59**, 1472 (2012).
11. Q. Zhang, M. Qu, X. Liu, Y. Cui, H. Hu, Q. Li, M. Jin, J. Xian, Z. Nie, and C. Zhang, *Advanced Materials Interfaces* **10**, 2201735 (2023).
12. F. J. Romero, E. Castillo, A. Rivadeneyra, A. Toral-Lopez, M. Becherer, F. G. Ruiz, N. Rodriguez, and D. P. Morales, *Npj Flexible Electronics* **3**, 1 (2019).
13. X. Xu, M. Luo, P. He, X. Guo, and J. Yang, *Appl. Phys. A* **125**, 714 (2019).
14. T. R. Ray, J. Choi, A. J. Bandodkar, S. Krishnan, P. Gutruf, L. Tian, R. Ghaffari, and J. A. Rogers, *Chem. Rev.* **119**, 5461 (2019).
15. J. Lin, Z. Peng, Y. Liu, F. Ruiz-Zepeda, R. Ye, E. L. G. Samuel, M. J. Yacamán, B. I. Yakobson, and J. M. Tour, *Nat Commun* **5**, 5714 (2014).
16. T.-S. D. Le, H.-P. Phan, S. Kwon, S. Park, Y. Jung, J. Min, B. J. Chun, H. Yoon, S. H. Ko, S.-W. Kim, and Y.-J. Kim, *Advanced Functional Materials* **32**, 2205158 (2022).
17. Y. Guo, C. Zhang, Y. Chen, and Z. Nie, *Nanomaterials* **12**, 2336 (2022).
18. M. G. Stanford, C. Zhang, J. D. Fowlkes, A. Hoffman, I. N. Ivanov, P. D. Rack, and J. M. Tour, *ACS Appl. Mater. Interfaces* **12**, 10902 (2020).
19. F. J. Romero, A. Salinas-Castillo, A. Rivadeneyra, A. Albrecht, A. Godoy, D. P. Morales, and N. Rodriguez, *Nanomaterials* **8**, 517 (2018).
20. S. S. Barold, *Card Electrophysiol Rev* **7**, 99 (2003).
21. E. Castillo, D. P. Morales, A. García, L. Parrilla, V. U. Ruiz, and J. A. Álvarez-Bermejo, *PLOS ONE* **13**, e0199308 (2018).
22. U. Satija, B. Ramkumar, and M. S. Manikandan, *BioCybernetics and Biomedical Engineering* **38**, 54 (2018).
23. I. R. Hristovski, L. A. Herman, M. E. Mitchell, N. I. Lesack, J. Reich, and J. F. Holzman, *Nanomaterials* **12**, 1241 (2022).
24. Y. Wang, Y. Wang, P. Zhang, F. Liu, and S. Luo, *Small* **14**, 1802350 (2018).
25. K. Rathinam, S. P. Singh, Y. Li, R. Kasher, J. M. Tour, and C. J. Arnsch, *Carbon* **124**, 515 (2017).
26. A. K. Thakur, B. Lin, F. H. Nowrin, and M. Malmali, *ACS EST Water* **2**, 75 (2022).
27. R. Ye, D. K. James, and J. M. Tour, *Acc. Chem. Res.* **51**, 1609 (2018).
28. J. B. In, B. Hsia, J.-H. Yoo, S. Hyun, C. Carraro, R. Maboudian, and C. P. Grigoropoulos, *Carbon* **83**, 144 (2015).
29. J.-W. Jeong, W.-H. Yeo, A. Akhtar, J. J. Norton, Y.-J. Kwack, S. Li, S.-Y. Jung, Y. Su, W. Lee, J. Xia, and others, *Advanced Materials* **25**, 6839 (2013).

30. A. Dallinger, K. Keller, H. Fitzek, and F. Greco, *ACS Appl. Mater. Interfaces* **12**, 19855 (2020).
31. F. J. Romero, D. Gerardo, R. Romero, I. Ortiz-Gomez, A. Salinas-Castillo, C. L. Moraila-Martinez, N. Rodriguez, and D. P. Morales, *Micromachines* **11**, 555 (2020).
32. M. Abdulhafez, G. N. Tomaraei, and M. Bedewy, *ACS Appl. Nano Mater.* **4**, 2973 (2021).
33. S. Bai, Y. Tang, L. Lin, L. Ruan, R. Song, H. Chen, Y. Du, H. Lin, Y. Shan, and Y. Tang, *Journal of Manufacturing Processes* **84**, 555 (2022).
34. S.-F. Tseng and Y.-S. Tsai, *Int J Adv Manuf Technol* **120**, 5351 (2022).
35. E. R. Mamleyev, S. Heissler, A. Nefedov, P. G. Weidler, N. Nordin, V. V. Kudryashov, K. Länge, N. MacKinnon, and S. Sharma, *Npj Flex Electron* **3**, 2 (2019).
36. K. C. Yung, D. W. Zeng, and T. M. Yue, *Applied Surface Science* **173**, 193 (2001).
37. E. E. Ortelli, F. Geiger, T. Lippert, J. Wei, and A. Wokaun, *Macromolecules* **33**, 5090 (2000).
38. J. E. Ferl and E. R. Long, *IEEE Transactions on Nuclear Science* **28**, 4119 (1981).
39. V. T. Nguyen, H. D. Le, V. C. Nguyen, T. T. T. Ngo, D. Q. Le, X. N. Nguyen, and N. M. Phan, *Adv. Nat. Sci: Nanosci. Nanotechnol.* **4**, 035012 (2013).
40. R. Murray, M. Burke, D. Iacopino, and A. J. Quinn, *ACS Omega* **6**, 16736 (2021).
41. K. Arquilla, A. K. Webb, and A. P. Anderson, in *2020 42nd Annual International Conference of the IEEE Engineering in Medicine & Biology Society (EMBC)* (2020), pp. 4498–4501.

Supporting Information

Optimization of Dry Laser-Induced Graphene (LIG) Electrodes for Electrocardiography (ECG) Signals Monitoring

Denice Gerardo^{1,3}, Yann Houeix¹, Francisco J. Romero¹, Carmen L. Moraila^{1,4}, Isabel Blasco-Pascual², María Pérez-Cadenas^{5,6}, Diego P. Morales¹, Noel Rodriguez¹, Alfonso Salinas-Castillo^{2,*}

¹ Dept. Electronics and Computer Technology, Faculty of Sciences, University of Granada, Granada 18071, Spain.

² Dept. Analytical Chemistry, Faculty of Sciences, University of Granada, Granada 18071, Spain.

³ Facultad de Biología, University of Sinaloa, Culiacan, 80040, Mexico.

⁴ Facultad de Ciencias Físico-Matemáticas, University of Sinaloa, Culiacan, 80040, Mexico.

⁵ Department of Inorganic Chemistry and Technical Chemistry, UNED, Madrid 28232, Spain.

⁶ Dept. Inorganic Chemistry, Faculty of Sciences, University of Granada, Granada 18071, Spain.

* corresponding author, alfonsos@ugr.es

Available ORCID List: D.G. 0000-0002-7810-6345; Y.H. 0000-0002-1959-2187; F.J.R. 0000-0002-1582-9626; C.L.M. 0000-0002-6659-7781; I.B.P. 0000-0003-3997-9191; M.P.C. 0000-0001-8377-587X; D.P.M. 0000-0002-3294-8934, N.R. 0000-0002-6032-6921; A.S.C. 0000-0002-1360-6699.

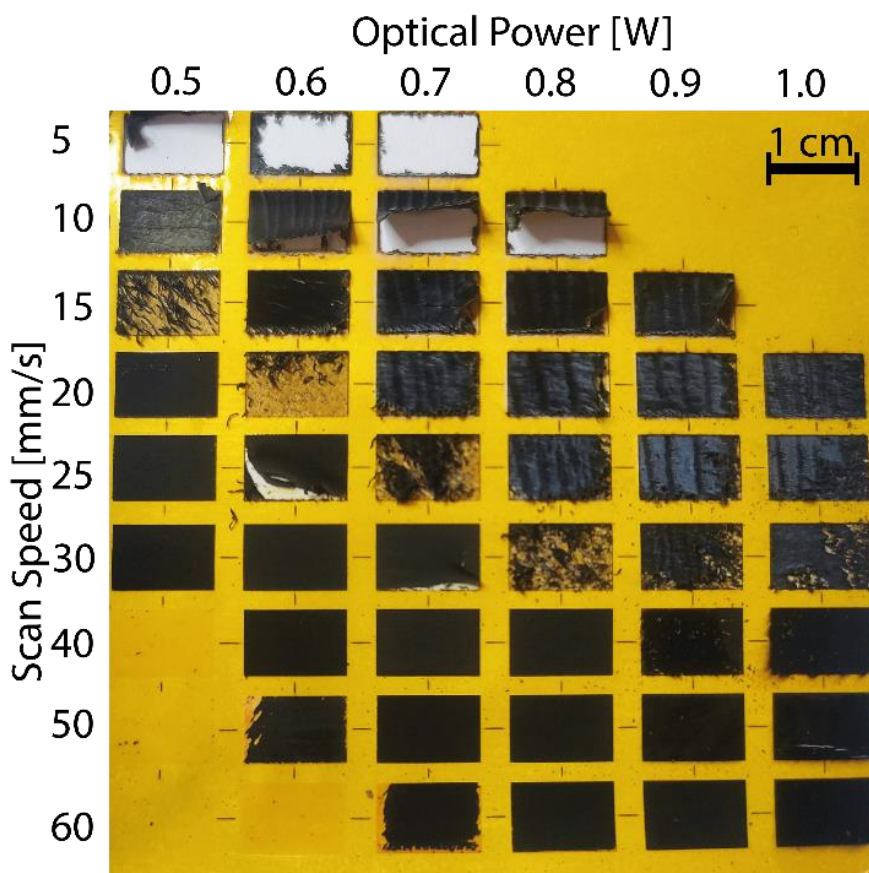


Fig. S1. LIG samples obtained at various laser power and scan speed conditions.

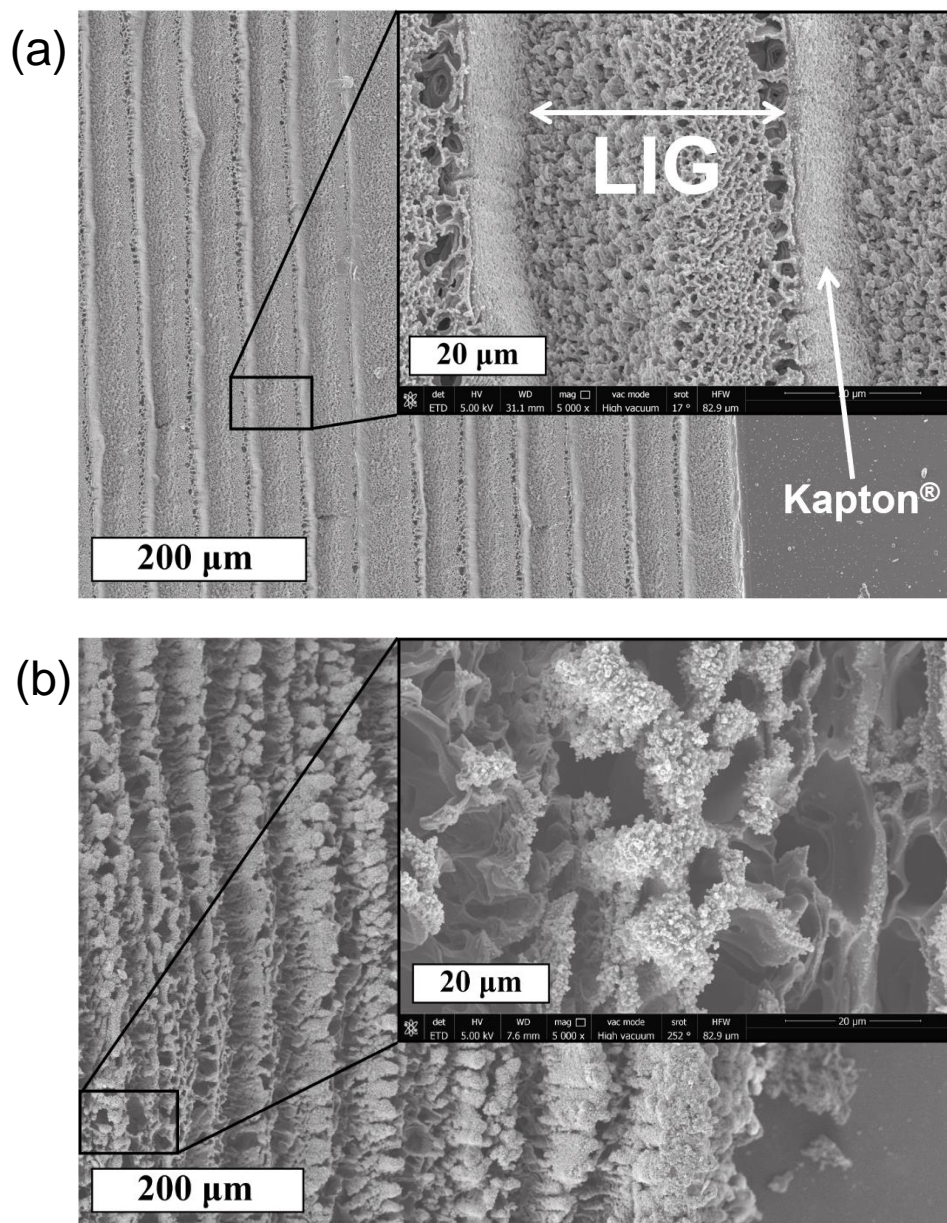


Fig. S2. Scanning Electron Microscope (SEM) images. (a) LIG obtained with a laser power of 0.6 W and a scanning speed of 50 mm/s. (b) (a) LIG obtained with a laser power of 0.7 W and a scanning speed of 15 mm/s.